

Wavelet analysis of millisecond variability of Cygnus X-1 during its failed state transition

Paweł Lachowicz¹* and Bożena Czerny¹

¹*Nicolaus Copernicus Astronomical Center, Bartycka 18, 00-716 Warszawa, Poland*

5 November 2018

ABSTRACT

Application of multi-resolution analysis adopting wavelets in order to investigate millisecond aperiodic X-ray variability of Cyg X-1 is presented. This relatively new approach in a time-series analysis allows us to study both the significance of any flux oscillations localized in time–frequency space, as well as the stability of its period. Using the observations of the *RXTE/PCA* we analyze archival data from Cyg X-1 during its failed state transition. The power spectrum of such a state is strongly dominated by a single Lorentzian peak corresponding to a damped oscillator. Our wavelet analysis presented in this paper shows the existence of short lasting oscillations without an obvious trend in the frequency domain. Based on this result, we suggest the interpretation of the dominant components of Cyg X-1 power spectrum in all spectral states: (i) a power law component dominating a soft state is due to accretion rate fluctuations related to MRI instability in the cold disk, (ii) the low frequency Lorentzian is related to the same fluctuations but in the inner ion torus, and (iii) the high frequency Lorentzian (dominating the power spectrum during the failed state transition) is due to the dynamical pulsations of the inner ion torus.

The usage of the wavelet analysis as a potential and attractive tool in order to spot the *semi-direct* evidences of accretion process onto black-holes is proposed.

Key words: accretion, accretion disks – binaries: general – stars: individual: Cyg X-1 – X-rays: observations – X-rays: stars.

1 INTRODUCTION

Cyg X-1 (Bowyer et al. 1965) belongs to the class of Galactic accreting black-hole binaries characterized by a highly variable X-ray emission in time-scales covering up to ten orders of magnitude (e.g. Nowak et al. 1999; Reig, Papadakis & Kylafis 2002; Psaltis 2004). The optical companion, HDE 226868 star (Bolton 1972; Webster & Murdin 1972) was classified as O9.7Iab supergiant (Walborn 1973) with the orbital period of 5.6 d. The main source of the matter accreting onto black hole is the focused stellar wind taking its origin from HDE 226868. Mass ranges of the components are $10\text{--}32 M_{\odot}$ and $16\text{--}55 M_{\odot}$ for the black-hole and the supergiant, respectively (Gies & Bolton 1986; Herrero et al. 1995; Ziolkowski 2005).

The power spectrum density (PSD) of the X-ray emission is broad-band and aperiodic. It was frequently characterized as a broken power-law (Sutherland, Weiskopf & Kahn 1978; Belloni & Hasinger 1990; Nowak et al. 1999; Revnivtsev, Gilfanov & Churazov 2000), with occasional

narrow quasi-periodic features (QPO) (Angelini, White & Stella 1992). Higher quality data allowed for more sophisticated parameterization of the PSD through a number of broad Lorentzians and a power-law component (e.g. Nowak 2000; Pottschmidt et al. 2003, hereafter P03). The lightcurve is not stationary. In short time-scales the variance is proportional to the mean luminosity of the source (Uttley & McHardy 2001; Gleissner et al. 2004) so the normalized power spectrum is broadly used to characterize the source (Miyamoto et al. 1992 and most of the subsequent papers). In long time-scales also the shape of the PSD changes as it depends significantly on the spectral state of the source (e.g. Cui et al. 1997a; 1997b).

Although frequently used, Fourier-based technique is actually not suitable for the analysis of the aperiodic variability. The Fourier analysis uses a fixed sinusoidal basis functions to decompose a signal. This method therefore provides excellent frequency resolution of persistent features but it fails when the signal is highly aperiodic and existing modulations are needed to be localized in time–frequency space.

To overcome this problem one needs to use a multi-

* E-mail: paulo@camk.edu.pl

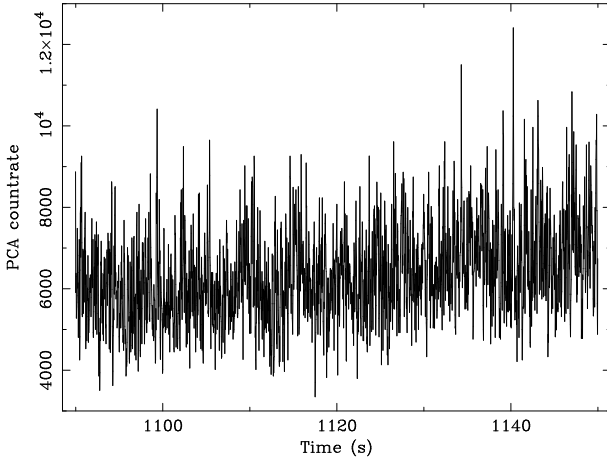


Figure 1. The lightcurve of Cyg X-1 as observed by the *RXTE/PCA* on 1999.12.05, showing a 60 s sequence of data selected by us for deeper studies using wavelet analysis.

resolution approach, e.g. by wavelet analysis (WA). Because the wavelet decomposition gives an idea of both the local frequency content of a time-series and the temporal distribution of these frequencies, its application in astronomical signal processing is increasing rapidly (e.g. Szatmary, Vinko & Gal 1994; Escalera & MacGillivray 1995; Frick et al. 1997; Aschwanden et al. 1998; Barreiro & Hobson 2001; Freeman et al. 2002; Irastorza et al. 2003). Interestingly, so far the application of wavelets in order to study variability of X-ray binary systems and active galactic nuclei was marginal. Scargle et al. (1993) used them to examine QPO and very low-frequency noise for Sco X-1 whereas Steiman-Cameron et al. (1997) supplemented Fourier detection of quasi-periodic oscillations in the optical lightcurves of GX 339-4 by scalograms, a wavelet technique. Fritz & Bruch (1998) applied this technique to the analysis of the optical luminosity variations in cataclysmic variables while Liszka, Pacholczyk & Stoeger (2000a) analyzed the ROSAT lightcurve of NGC 5548 in short time-scales.

In this paper we select a very special observation of Cyg X-1 performed on 1999.12.05. It was examined by P03 and the state of the source was described as failed state transition. The power spectrum at that time was particularly simple since the dominant part of the power was contained in a single Lorentzian peak. The aim of our paper is to verify with the wavelet analysis whether indeed a simple damped oscillator well represents the time-resolved lightcurve properties.

Our paper is organized as follows. Section 2 provides information on our data selection and reduction. In Section 3 we describe most essential aspects of the time-frequency analysis, starting from a brief discussion of computing X-ray power spectra and associated time-resolution problem. Next, we provide a description of calculation of a continuous wavelet transform in the frame of our interest. Section 4 contains the analysis of Cyg X-1 lightcurve whereas a discussion of results, including the lightcurve simulations, is the subject of Section 5. We conclude in Section 6.

2 DATA SELECTION AND REDUCTION

To probe the object variability in time-scales of seconds we use the observation by Proportional Counter Array on board of the *Rossi X-ray Timing Explorer (RXTE/PCA)*; Bradt, Rothschild & Swank 1993) taken from the public archive of the HEASARC. We select the PCA data set of 40099-01-24-01 (1999.12.05) on which we concentrate our investigation. The data were reduced with the LHEASOFT package v. 5.3.1 (May 2004) applying a standard data selection, i.e. the Earth elevation angle $> 10^\circ$, pointing offset $< 0^\circ.01$, the time since the peak of the last South Atlantic Anomaly SAA > 30 min and the electron contamination < 0.1 . The number of Proportional Counting Units (PCUs) opened during the observation was equal 3.

We extract the lightcurve in 2.03–13.1 keV energy band (channels 0–30) and rebin it with one common bin size value of $\Delta t = 0.025$ s. The average count-rate in this set is $\bar{x} = 6061.8$ cts s $^{-1}$ and the fractional rms 21.6 %. For needs of computation of the Fourier power spectra, we use POWSPEC software with an applied Poisson noise level subtraction. For purposes of wavelet analysis, the IDL software provided by Torrence & Compo (1998) (hereafter TC98; see Acknowledgments for the URL address) was run.

3 TIME-FREQUENCY ANALYSIS

Computation of the Fourier power spectral density is an ideal tool for detecting periodic fluctuations in the time-series. Therefore, in the absence of major problems caused by a window pattern (aliasing) and at high signal-to-noise ratio, a strong peak in the Fourier spectrum has an immediate interpretation (e.g. Gray 1976).

However, the Fourier analysis fails when time evolution of spectral features has to be taken into account. In order to capture this effect one needs to apply a time-frequency representation of the signal. The simplest solution to this problem is the application of Windowed Fourier Transform (see e.g. Cohen 1995; Flandrin 1999 for review). More advanced methods include inter alia Wigner-Ville distribution, the reassignment method or the Gabor spectrogram (see Vio & Wamsteker 2002 and references therein for a nice review). In the present paper we apply the alternative approach: the wavelet analysis.

3.1 Fourier power spectrum

For a reference, we calculate the PSD of the studied lightcurves using a standard approach (see van der Klis 1989 for review). We use the normalization of Miyamoto et al. (1992) which gives the periodogram in units of $(\text{rms}/\text{mean})^2/\text{Hz}$. Therefore, the integrated periodogram yields the square of fractional rms of a lightcurve. We subtract the noise as in Vaughan et al. (2003), omitting the correction for dead-times (see Zhang et al. 1995 for the discussion of the dead-time effect), as our data sets are rather short (20 s) and thus the uncertainty in the determination of the PSD dominates.

3.2 Wavelet analysis

A basic concept standing for its application to the time-series was to analyze the signal at different frequencies with different resolutions (see e.g. Farge 1992; Daubechies 1992 and TC98 for good summary on wavelets). Contrary to the Fourier transform, the wavelet analysis makes use of a set of functions, *wavelets*, which are localized in scale–time space¹. Several standard shapes are broadly used, depending on the subject under study.

3.2.1 Wavelets

The basic concept is a mother wavelet function, $\psi(t)$, which depends on time-parameter t . A wavelet's family is therefore generated by scaling and shifting of $\psi(t)$ as follows:

$$\psi_{a,b}(t) = \frac{1}{\sqrt{a}} \psi\left(\frac{t-b}{a}\right) \quad a, b \in \mathbb{R}, a > 0 \quad (1)$$

where a and b are factors standing for scaling and time-shifting, respectively.

There are three most commonly used wavelets in the astronomical time-series analysis: (a) a Marr or Mexican Hat:

$$\psi_{\text{Marr}}(t) = (1 - t^2)e^{-t^2/2}, \quad (2)$$

(b) a Morlet wavelet:

$$\psi_{\text{Morlet}}(t) = \pi^{-1/4} e^{i2\pi\nu_0 t} e^{-t^2/2} \quad (3)$$

which has the complex sinusoidal waveform confined by the Gaussian bell envelope (Grossman & Morlet 1984), and (c) a Paul wavelet:

$$\psi_{\text{Paul}}(t) = \frac{2^m i^m m!}{\sqrt{\pi(2m)!}} (1 - it)^{-(m+1)} \quad (4)$$

where m denotes an order (Paul 1984; Combes, Grossmann & Tchamitchian 1989). These functions are presented in Fig. 2. Application of complex wavelets instead of real-valued ones is required to capture information on the amplitude and phase simultaneously. On the other hand, a real-valued functions are useful for isolation of positive and negative modulations as the separate peaks in the time–scale plane, making a clear discrimination of the sharp features and the signal discontinuities possible to resolve.

In our research we are mainly interested in detection and studies of aperiodic flux structures, therefore the Morlet wavelet (with $2\pi\nu_0 = 6$) will be used throughout the paper. As it oscillates due to a term of e^{it} and owns a complex form it becomes a desired probing tool in tracing and quantifying quasi-periodic modulations at different scales.

3.2.2 Wavelet power spectrum

For discretely defined time-series x_k , $k = 0, \dots, N_{\text{obs}} - 1$, the wavelet transform can be denoted in its discrete form as:

$$w_k(a) = \sqrt{\frac{\Delta t}{a}} \sum_{k'=0}^{N_{\text{obs}}-1} x_{k'} \psi^* \left[\frac{(k' - k)\Delta t}{a} \right] \quad (5)$$

¹ In the wavelet analysis a term *scale* is used instead of *frequency* which is reserved for the Fourier analysis.

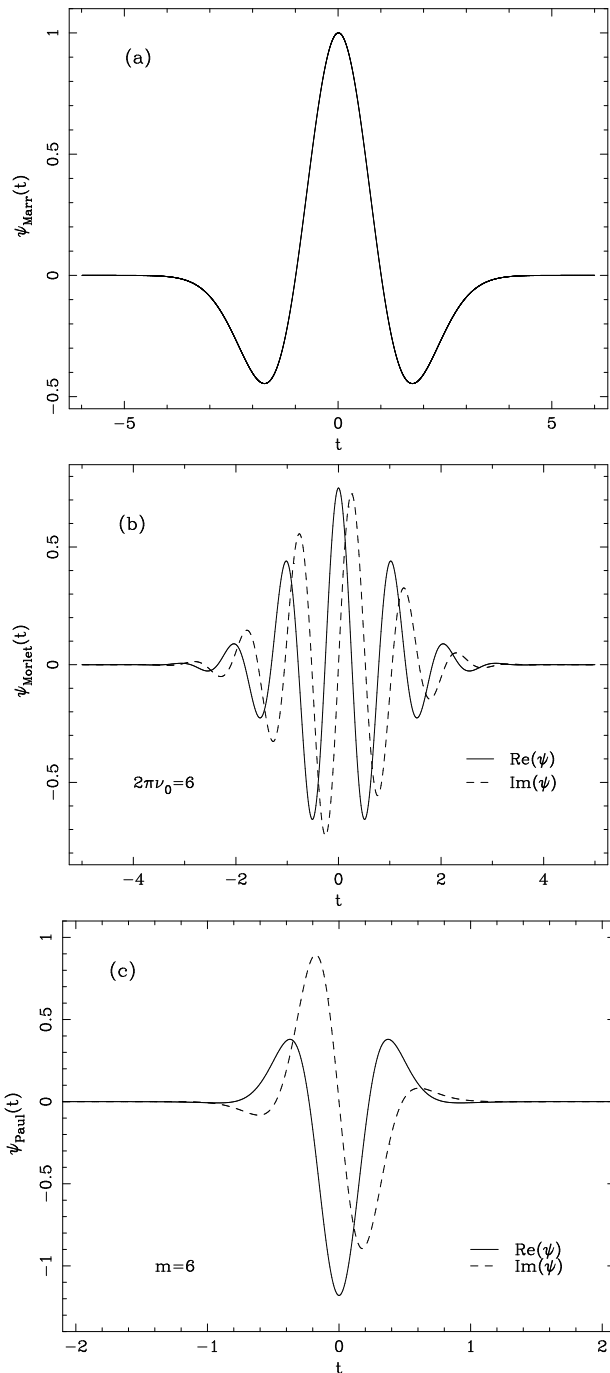


Figure 2. Examples of mother wavelets: (a) Marr wavelet; (b) Morlet wavelet; (c) Paul wavelet. The real and imaginary parts of complex wavelets were plotted by solid and dashed lines, respectively.

where Δt is the sampling time of a lightcurve, k represents a localized time index and a factor of $\sqrt{\Delta t/a}$ ensures that the wavelet contains the same energy everywhere in time–scale space of $w_k(a)$ coefficients. In practice, there is no need to use formula (5) for the calculation of wavelet transform. It can be expressed in terms of the inverse Fourier transform of the product of the Fourier transforms of the signal and wavelet function as given by equation (A11) and therefore allow to speed up the calculations.

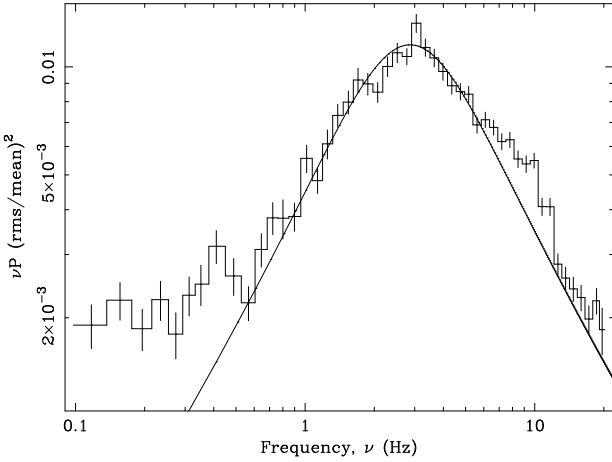


Figure 3. Fourier power spectrum of Cyg X-1 on Dec 5, 1999. Solid line represents a broad Lorentzian peak fitted by Pottschmidt et al. (2003).

A *wavelet power spectrum* can be simply defined as normalized square of the modulus of the wavelet transform:

$$W = \xi |w_{a,b}|^2 \equiv \xi |w_k(a_m)|^2. \quad (6)$$

A choice of a normalization factor can be done arbitrarily where the most convenient way is to set $\xi = \sigma^{-2}$, i.e. equal to the inverse square of the lightcurve variance. Here, σ^2 represents the expectation value of the wavelet transform for a white-noise process at each scale a_m and a time location k (TC98). The local wavelet power spectrum W with $\xi = \sigma^{-2}$ is distributed as χ^2_2 , i.e. as χ^2 distribution with two degrees of freedom, therefore it allows to determine the contours at given confidence level for every flux oscillation. A reality of any peak in the wavelet map is tested against certain background spectrum and thus any peak can be accepted or rejected at earlier assumed significance level.

Due to a finite duration of a lightcurve some artifacts may appear at the edges of the wavelet maps. To force them to be negligible one may introduce a *cone of influence* defined as a region of the wavelet map where a wavelet power in the vicinity of signal discontinuity decreases by the factor of e^{-2} (TC98).

2-D information about the signal in the wavelet map also allows us to compare it to the results of Fourier power spectrum. It can be achieved by performing an integration of the wavelet spectrum over time which is known under the name of a *global wavelet (power) spectrum* or a *scalegram* technique (Scargle et al. 1993). Its discrete form can be denoted as:

$$G(a_m) = \frac{\xi}{N_{\text{obs}}} \sum_{k=k_1}^{k_2} |w_k(a_m)|^2 \quad (7)$$

where $0 \leq k_1 < k_2 \leq N_{\text{obs}} - 1$ and ξ denotes the normalization factor. Here, k_1 and k_2 ought to be chosen to lie outside the cone of influence for particular scale a_m . Since the normalization can be arbitrary, one can choose it the same as for the wavelet power spectrum (e.g. $\xi = \sigma^{-2}$) and therefore determine the proper significance levels (see TC98 for details). If so, when a comparison of (7) with the calculated Fourier power spectrum is required, it is possible to adopt a normalization factor of the wavelet spectrum $\xi = 2\Delta t/\bar{x}^2$.

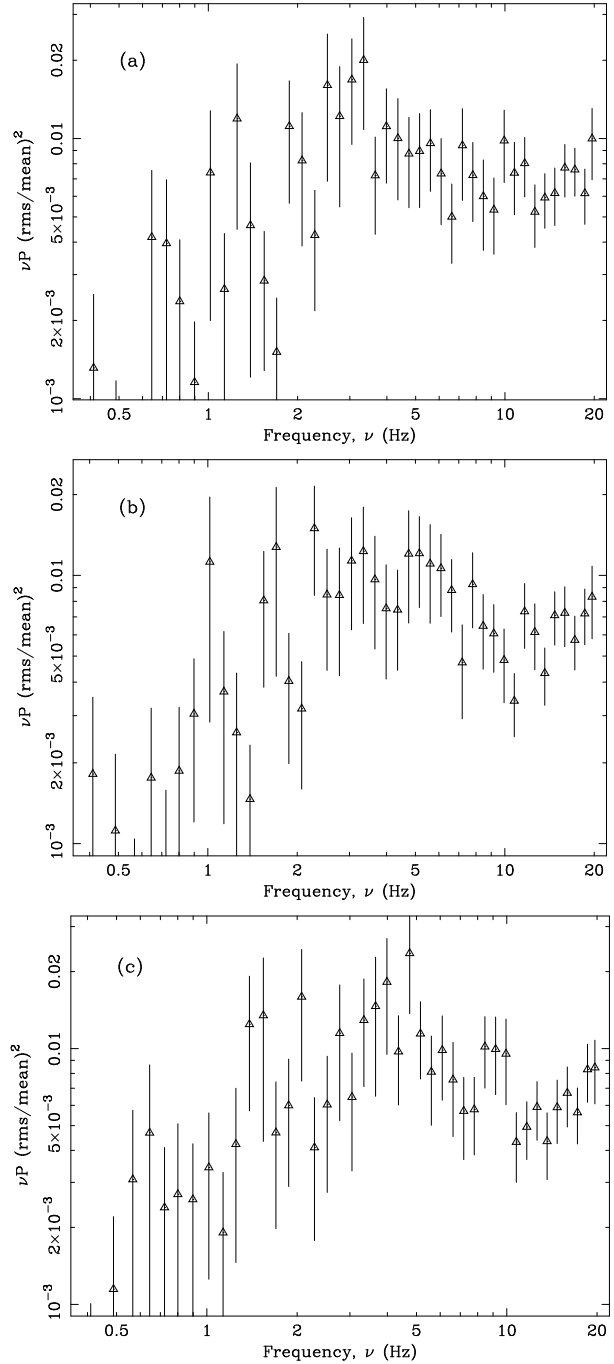


Figure 4. Exemplary power spectra calculated for the single consecutive data streams of duration 20 s corresponding to the PCA lightcurve intervals: (a) 1090–1110 s, (b) 1110–1130 s, (c) 1130–1150 s. For purposes of a comparison with the global wavelet power spectra in Fig. 5, the subtraction of a noise level was not applied.

Thus, the global wavelet power spectrum will have the units of $(\text{rms}/\text{mean})^2/\text{Hz}$.

A relation between the wavelet scale a and the Fourier frequency ν depends on our choice of the wavelet function. For the Morlet function ($2\pi\nu_0 = 6$) it holds $\nu_{\text{Morlet}} \simeq (1.03a)^{-1}$, for the Marr wavelet $\nu_{\text{Marr}} \simeq (3.97a)^{-1}$ whereas for the Paul wavelet ($m = 6$) $\nu_{\text{Paul}} \simeq (0.97a)^{-1}$. Hereafter,

y-axes for all of our wavelet maps will be expressed as frequency, given by the above transformations.

4 RESULTS

The selected data set covers 1364 s. In Fig. 3 we show the corresponding PSD, together with the dominant Lorentzian component fitted by P03. The shape of the Lorentzian component was described as:

$$L_2(\nu) = \pi^{-1} \frac{2R_2^2 Q_2 \nu_2}{\nu_2^2 + 4Q_2^2(\nu - \nu_2)^2}, \quad (8)$$

and the best fit values of the parameters were: amplitude $R_2 = 0.188 \pm 0.004$, center frequency $\nu_2 = 1.769^{+0.066}_{-0.070}$ Hz, and the quality factor $Q_2 = 0.395^{+0.032}_{-0.035}$. This power spectrum component has a maximum at the frequency 2.856 Hz, and a characteristic decay time-scale, $\tau_2 = Q_2/(\pi\nu_2)$, is given by $\tau_2 = 0.07$ s.

The presented PSD shows relatively small errors since the whole time sequence was used. The whole lightcurve was divided into intervals of 25.6 s, the PSD was calculated for each part separately, and finally averaged PSD was plotted, as customary done for such data.

When single PSD spectra are not averaged, they show a considerable scatter. This scatter is expected from the χ^2 distribution of the individual PSD values. For the purpose of further discussion of the wavelet maps, we show (see Fig. 4) the examples of the PSD obtained for the single fragments of the lightcurve of duration 20 s. Errors are large but the Lorentzian shape is still visible. The selection of 60 s long sequence from whole duration of our PCA time-series was done by us randomly, here corresponding to the interval between 1090–1150 s (Fig. 1).

4.1 Wavelet maps

We construct the wavelet maps for the same parts of the lightcurve as used in the PSD analysis. The selected band of scales corresponds to the Fourier frequency range between 1 and 10 Hz, where the Lorentzian has the maximum.

We use the Morlet wavelet, with the standard assumption $2\pi\nu_0 = 6$ (see Section 3.2.1). This means that we probe the signal with a damped wave performing ~ 3 oscillations.

The result is shown in Fig. 5, for three consecutive parts of the lightcurve. Integrated wavelet spectra are shown to the right of each of the sequences.

In all maps many localized strong peaks are seen, standing clearly out of the background. This is even better seen in a 3-D plot (see Fig. 6, upper panel). Those peaks dominate the integrated spectrum although they are present only occasionally, mostly between 2–5 Hz. Many lower but still significant peaks are also present, so active phase with significant peaks covers more than half of the observed time. No single frequency seems to be favored and we do not see any particular evolutionary trend. The largest peaks extend in time typically for ~ 1 s which means that they are practically unresolved. Those which extend for a few seconds can be elongated either in the direction of lower or higher frequencies, and the shapes are rather irregular.

We analyzed the distribution and the properties of the

Table 1. Properties of the localized peaks in the wavelet maps for the assumed significance level of 90%.

Sequence	Cyg X-1	Simulated lightcurve (equation 9)
<i>Number of localized peaks</i>		
Seq. 1	18	11
Seq. 2	16	16
Seq. 3	17	12
<i>Activity level, κ, in %</i>		
Seq. 1	63.6	51.2
Seq. 2	59.9	59.5
Seq. 3	62.3	67.9
<i>Median of peak duration, ΔT_p, in [s]</i>		
Seq. 1	0.54	0.54
Seq. 2	0.54	0.45
Seq. 3	0.27	0.54
<i>Median of peak width, $\Delta \log \nu_p$</i>		
Seq. 1	0.12	0.13
Seq. 2	0.14	0.11
Seq. 3	0.14	0.15
<i>Median of peak frequency, ν_p, in [Hz]</i>		
Seq. 1	3.7	3.9
Seq. 1	4.3	3.8
Seq. 3	5.2	2.8
<i>Peak width, $\Delta \log \nu_h$, of the highest peak</i>		
Seq. 1	0.25	0.23
Seq. 2	0.21	0.35
Seq. 3	0.39	0.47
<i>Peak duration, ΔT_h, of the highest peak in [s]</i>		
Seq. 1	1.1	1.2
Seq. 2	2.8	1.6
Seq. 3	2.7	2.7
<i>Peak frequency, ν_h, of the highest peak in [Hz]</i>		
Seq. 1	3.4	2.2
Seq. 2	2.1	1.7
Seq. 3	1.4	1.5

significant peaks present in the observational data. The results are given in Table 1. For the analysis, we took only those peaks which are well determined, i.e. detected with 90% confidence level and not extending beyond the studied frequency range. We give there the number of such localized peaks in each of the three sequences. We define the activity level, κ , in each sequence as the fraction of time when at least one peak at any frequency is present. We determine the median value of the logarithm of the frequency, $\Delta \log \nu_p$, the median of the peak duration, ΔT_p , and the median of the peak frequency, ν_p . We also choose the highest of the peaks in each sequence and give for such peak its duration, ΔT_h , frequency ν_h , and uncertainty of its localization, $\Delta \log \nu_h$.

We see that most of the peaks are practically unresolved since their duration and the uncertainty of the frequency is comparable to the Heisenberg limits of the wavelet analysis. For the Morlet wavelet with $2\pi\nu_0 = 6$ the minimum value of $\Delta \log \nu = 0.11$, and the minimum value of the time resolution is 0.24 s at 3 Hz (0.71 s at 1 Hz and 0.07 s at 10 Hz). The count rate of the source is high (~ 6000 cts s^{-1}) which allows to reach the formal limit of the adopted approach.

Searching the whole lightcurve we have found several interesting sequences. One of them is shown in Fig. 7. There seems to be a chain of peaks, systematically moving towards higher frequencies. Such a development could be consistent with propagation of the perturbations towards the gravity

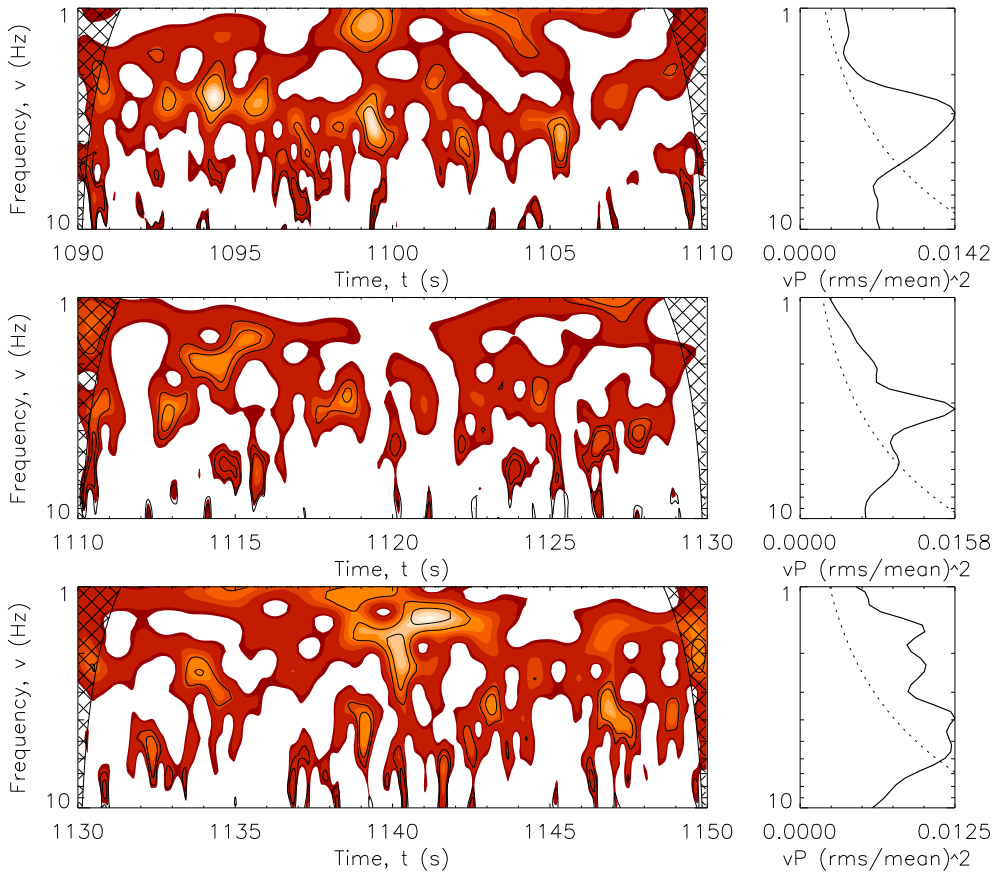


Figure 5. (Left panels) Wavelet power spectra of Cyg X-1 during its failed state transition on 1999.12.05 mapping a time-frequency evolution of ~ 3 Hz quasi-periodic feature (calculated for randomly selected 60 s time interval from the PCA time-series). Top values of wavelet power are denoted by gradual brightening of the color. Black solid contours denote significance level of 90% (outer) and 99% (inner) for detected peaks. 3-D visualization of the 1090–1110 s wavelet map is shown in Fig. 6. A cone of influence is marked as dashed region. (Right panels) Corresponding global wavelet power spectra, drawn as integrated over time wavelet power spectrum multiplied by the frequency (see Fig. 4 for a comparison with the Fourier PSD of the same time sequences). Dotted lines represent the 95% significance level calculated according to the procedure given in TC98.

center, with the expected time-scales decreasing with the radius. We discuss it in Section 5.8.

For the purpose of a comparison, the contours corresponding to 99% significance level were drawn additionally on the wavelet maps. We found that at this level of significance only the most prominent features of the local time-frequency variability are still detected. They cover a relatively small fraction of time in comparison to 90 % contours, with larger differences between the consecutive time sequences. Therefore, it seems that 90% contours are more convenient for characterizing the activity level, κ , of the lightcurve, whereas 99% contours should be used in verification of any trends in the frequency domain.

5 DISCUSSION

The nature of the short time-scale variability in X-ray emission of accreting binaries is still under discussion. The PSD is generally broad-band so the variability is successfully modeled as a shot noise (Terrell 1972; Lehto 1989). Later, more specific models with some physical background were developed (disk turbulence, Nowak & Wagoner 1995; magnetic

flares in the disk corona, Poutanen & Fabian 1999, Źycki 2002; propagation of perturbations in the inner hot flow, Böttcher & Liang 1999, Źycki 2003; perturbations in the accretion rate in the cold disk, Mineshige, Ouchi & Nishimori 1994, Lyubarskii 1997). Differentiation between those models is very difficult.

Occasionally, the power spectrum shows a hint of a single oscillation which dominates the variability. Such a situation happens during a transition state. Careful study of this apparently simple state should reveal the nature of variations more easily. For example, during a failed transition state, the PSD of Cyg X-1 was quite well represented by a single Lorentzian peak (P03).

Such a single Lorentzian peak represents a damped coherent oscillation with a time-independent frequency. This damping is responsible for the width of the peak. However, similarly broad power spectrum can in principle result from oscillations which are not so strongly damped but which change the frequency with time, like in case of a chirp signal (see e.g. Cohen 1995). Such a change in oscillation frequency may be, for example, connected with the accretion process: if the wave or hot plasma moves inward, the local characteristic scales may decrease with radius.

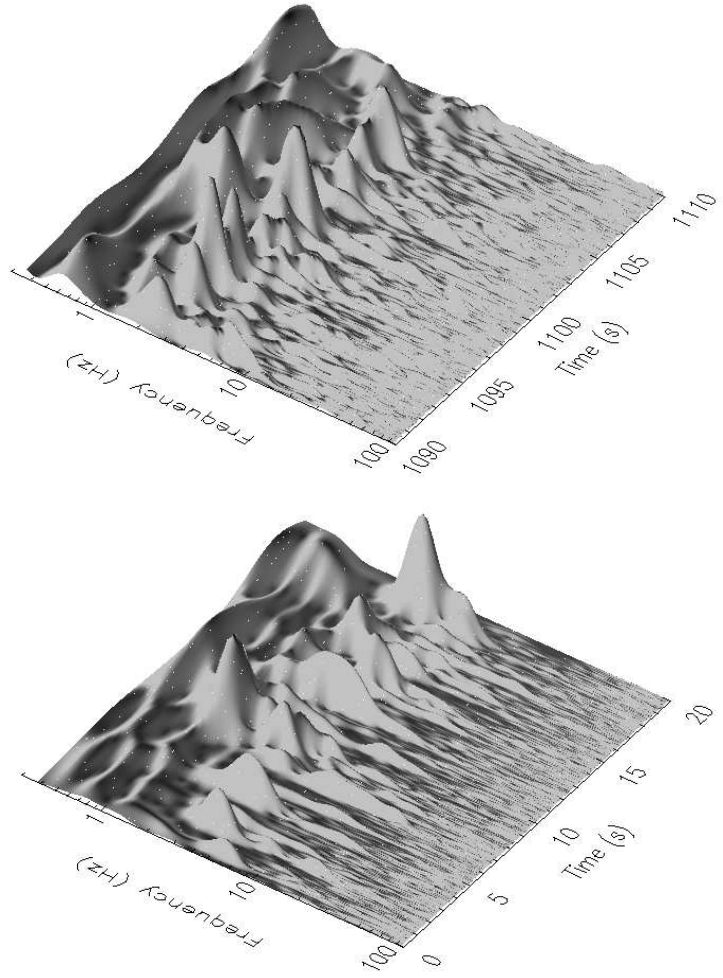


Figure 6. 3-D presentation of the wavelet power spectrum: (upper) for 20 s long PCA lightcurve; (bottom) for 20 s segment from a simulated lightcurve containing randomly occurring flares characterized by the Lorentz profile (see Section 5.1). In order of visualization of wavelet power distribution up to 100 Hz, maps were calculated for the lightcurves with the bin time of $\Delta t = 2^{-9}$ s.

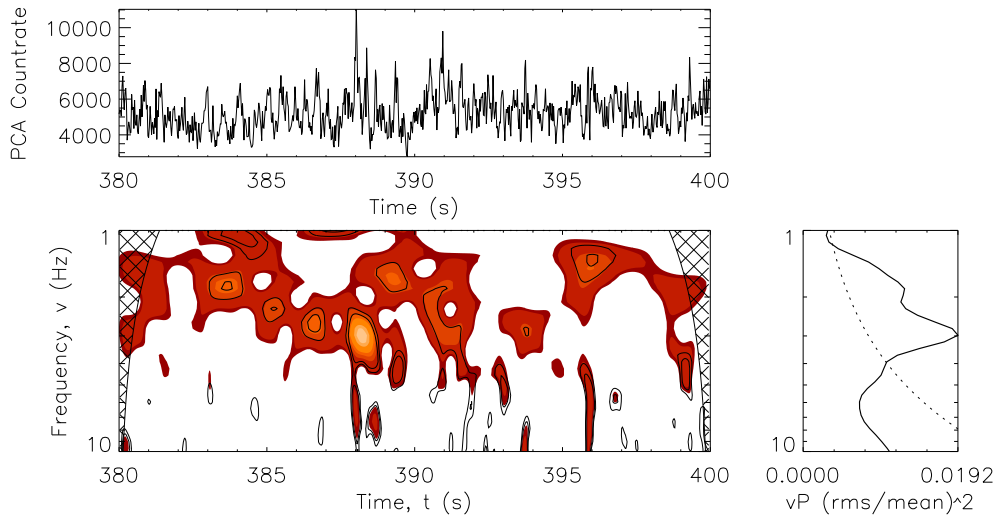


Figure 7. (Central panel) Wavelet power spectrum of Cyg X-1 revealing a puzzling chain of peaks ranging between 383–391 s of the analyzed PCA lightcurve (top panel). In the right, corresponding global wavelet power spectrum. See Section 5.8 for discussion.

The Fourier analysis cannot differentiate between the damped oscillation and the modulated frequency. Therefore, in order to search for the underlying physical process we need more advanced method of the analysis.

In this paper we applied wavelet analysis to the Cyg X-1 lightcurve. The wavelet maps show that strong, well localized oscillations are present rather occasionally, at frequencies $\sim 3\text{--}5$ Hz and they typically last for $\sim 0.3\text{--}0.5$ s. A few such strong peaks are always present in each of the 20 s sequences and they effectively determine the character of variability, although some peaks above the 90% confidence threshold are typically seen for more than half of the observation time. We did not find any systematic frequency change in oscillations. The analysis gave an upper limit on the rate of the frequency change during a single oscillation $\delta \ln \nu_0 / \delta \ln t \leq 0.2$.

This result supports the option of a coherent oscillation with strong damping present in the system. However, in order to analyze more qualitatively the description of the system as a damped oscillator we performed numerical simulations.

5.1 Lightcurves simulated in time domain

In order to model the observed lightcurve dominated by the Lorentzian peak we basically follow the approach of Źycki (2003). We create a simulated lightcurve as a superposition of the random shots with the shape:

$$F(t) = A_i e^{-(t-t_i)/\tau} \cos[2\pi\nu_2(t-t_i) + \phi_i] \quad \text{for } t > t_i, \quad (9)$$

and $F(t) = 0$ for $t < t_i$. The values of the frequency ν_2 and of the characteristic time-scale τ were fixed, i.e. the same for all shots. The amplitude of a shot, A_i , was assumed to cover uniformly the range between 0 and A_0 , the shot phase, ϕ_i , was assumed to be distributed uniformly between 0 and 2π . The moments of shot appearance, t_i , were chosen from the Poisson distribution, for an assumed mean frequency of shot generation, λ . It means that the time separation between the consecutive flares, $\delta t = t_{i+1} - t_i$, was given by $\delta t = -\log(\text{rand})/\lambda$ where rand is a random number between 0 and 1.

It is easy to show that such a lightcurve is characterized by a power density spectrum:

$$\mathcal{P}(\nu) = \frac{C}{\tau^{-2} + 4\pi^2(\nu - \nu_2)^2} + \frac{C}{\tau^{-2} + 4\pi^2(\nu + \nu_2)^2} \quad (10)$$

The first term has the Lorentzian shape, as requested. The second term is a smooth and slowly varying function so the sum of these two terms roughly preserves the Lorentzian shape. We cannot have a better representation of a Lorentzian power spectrum since the power spectrum of a real function in the time domain must have a power spectrum symmetric in the frequency. The Lorentzian shape itself is not symmetric so it corresponds to unphysical complex function in the time domain.

This complication means that formally we cannot use the published values of the Lorentzian peak's parameters in order to generate the simulated lightcurves with the same power spectrum. Instead, we should refit the original power spectrum with the new function given by equation (10). Since this shape is not strongly different from a Lorentzian (see Fig. 8), it represents the data equally well. The new

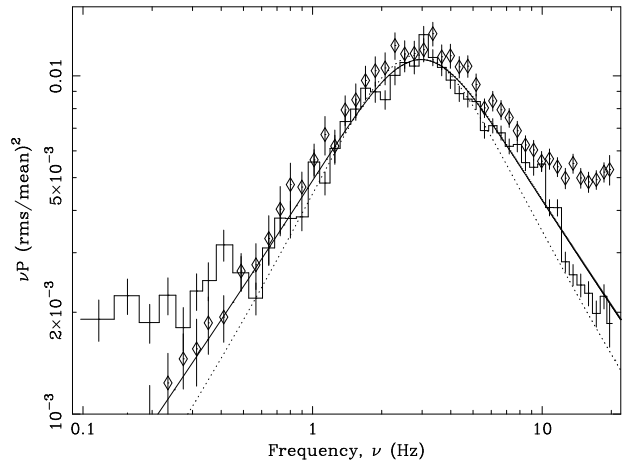


Figure 8. Comparison of the fits to the PCA power spectrum performed by Pottschmidt et al. (2003) (dotted line) and provided by the application of equation (10) (solid line). Diamond markers denote power spectrum calculated from 1000 s long simulated lightcurve (see Section 5.1).

values of the constants involved are: $C = 0.945 \pm 0.065$, $\nu_2 = 1.817 \pm 0.184$ Hz, $\tau = 0.067 \pm 0.003$ s. New value of the frequency and the damping time-scale are only slightly different from the values obtained by P03 from fitting a single Lorentzian peak (1.769 Hz and 0.07 s, correspondingly).

The lightcurve given by equation (9) has statistically zero mean so we must add the value representing the mean count rate, \bar{x} , in the PCA observation. The coefficients A_0 and λ must be chosen in such way that the resulting lightcurve has the required rms, the same as PCA data. Interestingly, we found that there exists a whole family of parameters (A_0, λ) which reproduce the required normalization of the power spectrum since the constant C in equation (10) is given by:

$$C \propto \frac{A_0^2 \lambda}{\bar{x}^2} \quad (11)$$

what implies that the following relation:

$$A_0^2 \lambda = \text{const} \quad (12)$$

holds for every couple of (A_0, λ) at assumed mean count rate, \bar{x} , and fractional rms variability.

We also included the white noise in our simulated lightcurve. For this purpose, in each of the time bins of the simulated time-series we calculate the number of photons, we treat this value as 'average', draw an actual number of counts from the Poisson distribution around this value and finally we divide this value by the bin size in order to return to count per second units. It can be shortly written as:

$$F_N(t) = \text{POISDEV}[F(t)\Delta t]/\Delta t. \quad (13)$$

Above, $F(t)$ is given by equation (9), POISDEV represents a subroutine which generates a random number with the Poisson distribution (Press et al. 1992) and thus $F_N(t)$ denotes simulated lightcurve with the Poisson noise level included.

The level of noise does not depend on a specific choice of a pair (A_0, λ) if it satisfies the relation (12). However, created lightcurves differ visually: low λ s naturally result in rare steep peaks while high λ s give apparently very noisy

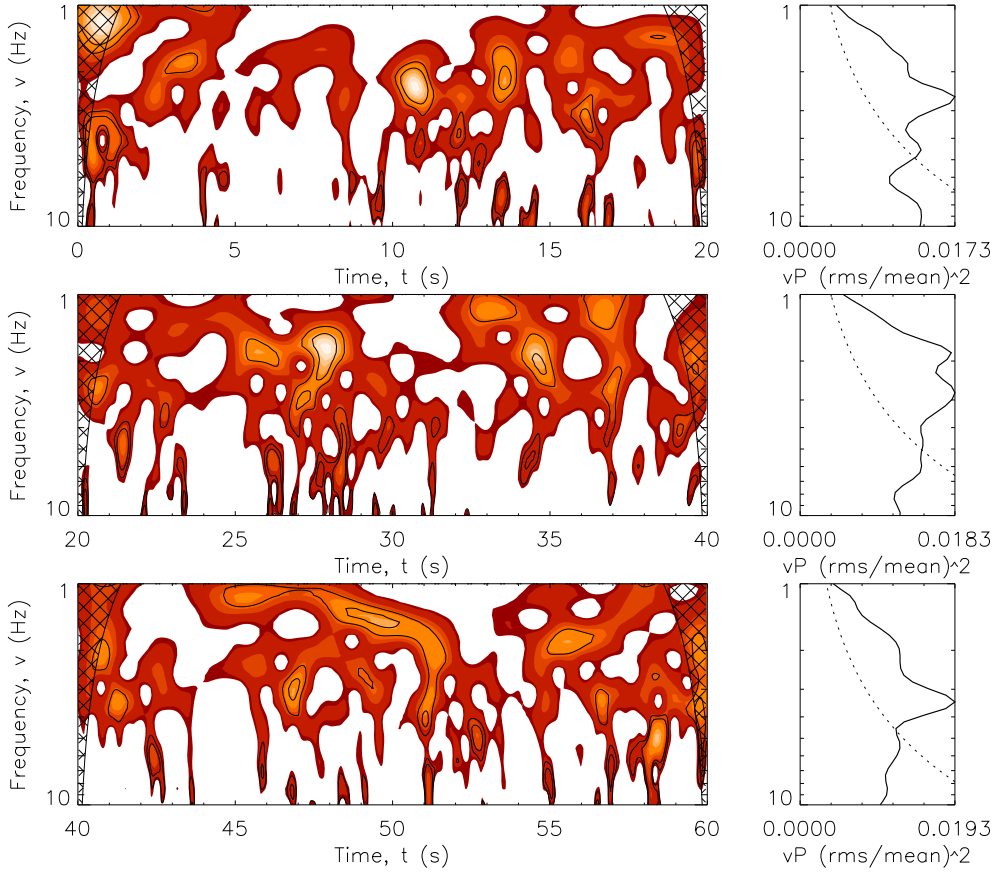


Figure 9. (Left panels) Wavelet power spectra of the simulated lightcurve ($\lambda = 20$, $A_0 = 2500 \text{ cts s}^{-1}$) calculated for randomly selected 60-second time interval. Top values of the wavelet power are denoted by gradual brightening of the color. Black solid contours denote significance level of 90% (outer) and 99% (inner) for detected peaks. A cone of influence is marked as dashed region. (Right panels) Corresponding global wavelet power spectra, drawn as integrated over time wavelet power spectrum multiplied by the frequency. Dotted lines represent the 95% significance level.

curve without clear pattern. Visually, lightcurves created with $\lambda \sim 20-30$ look most similar to the observed lightcurve of Cyg X-1. We will return to this point later.

5.2 Wavelet maps for simulated lightcurves

We generated 1000 s long lightcurve, $F_N(t)$, with assumed parameters: $\tau = 0.067$ s, $\lambda = 20$, $A_0 = 2500 \text{ cts s}^{-1}$ and $\nu_2 = 1.817$ Hz. The mean countrate of our simulated time-series yielded to be equal $6081.8 \text{ cts s}^{-1}$ whereas fractional rms 21.9%. In the first step we computed PSD to check whether such composed lightcurve is able to reproduce observed shape of power spectrum from the PCA data. Result of it has been presented in Fig. 8 by the diamond markers. As one can see, the shape and the width of PSD of simulated time-series agrees very well with the main spectral component of Cyg X-1 PSD.

Next, from $F_N(t)$ we again chose randomly three sequences, 20 s each, for the wavelet analysis. The wavelet maps for the simulated lightcurve are shown in Fig. 9. 3-D picture of exemplary series is shown in the bottom panel of Fig. 6.

The maps are very similar to those obtained from the data analysis. This can be even better seen from the quan-

titative parameters given in Table 1. Peaks in the maps for simulated lightcurves also are distributed in a broad frequency range.

At first glance this result may seem puzzling. Since the basic frequency in the simulated lightcurve is fixed, we might expect better localization of the peaks in frequency. However, the random choice of the phase, together with extremely strong damping, creates an apparent diversity of the shapes among the consecutive shots, leading to relatively broad peaks, at broad frequency range, as in the data.

Closer inspection suggests also certain systematic differences. Simulated lightcurves create slightly fewer peaks in the maps, and the median frequency in the data is somewhat higher. This is most probably related to an excess of the power at high frequencies above a single Lorentzian peak seen in the data ($\sim 8-12$ Hz, see Fig. 3). Otherwise, all properties of the observed lightcurve are well represented.

We also analyzed simulated lightcurves assuming lower and higher values of λ (with appropriate A_0 given by relation (12)). Maps for significantly larger or significantly smaller values of λ were different from the maps for Cyg X-1. Most noticeably, the activity level shortened to 45% for $\lambda = 5$ and 55% for $\lambda = 55$; it was 59.5% for $\lambda = 20$ and 61.9% in the

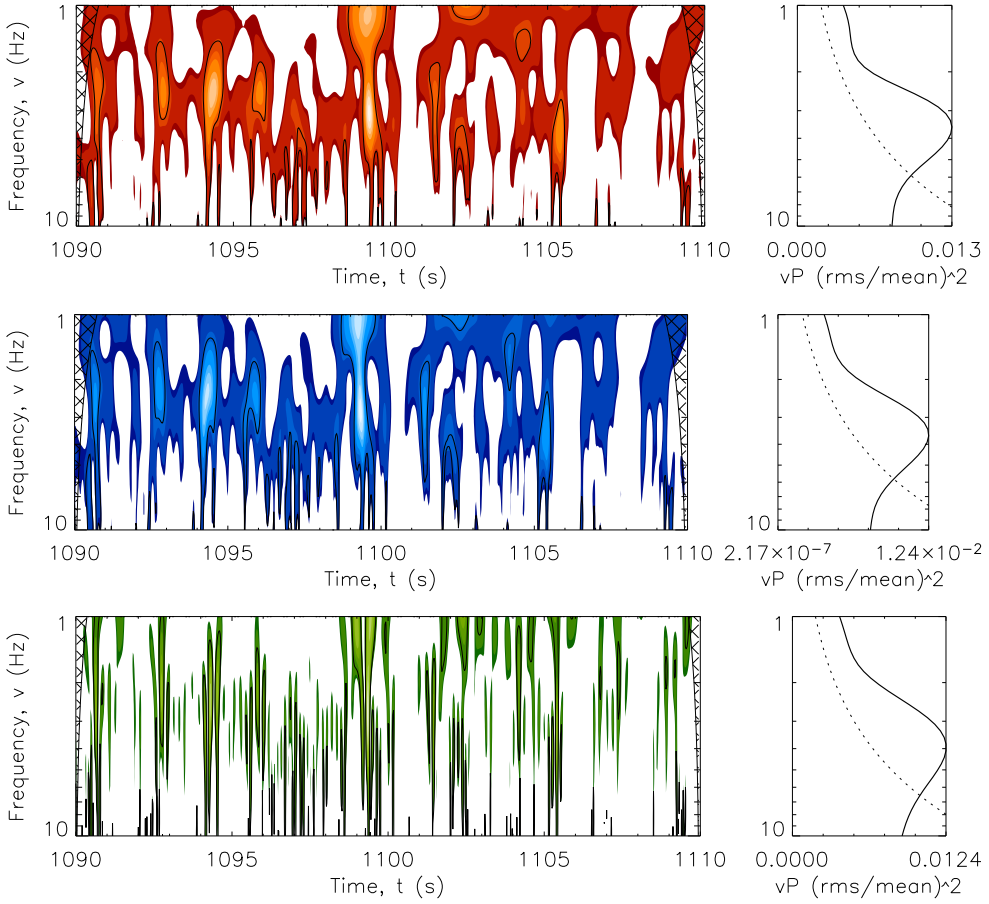


Figure 10. Wavelet power spectra of Cyg X-1 corresponding to the PCA data sequence between 1090–1110 s, calculated applying (top panel) Morlet wavelet with $2\pi\nu_0 = 3$, (middle panel) Paul wavelet with $m = 6$ and (bottom panel) Marr wavelet. In the right, corresponding global wavelet power spectra.

data maps. Therefore, wavelet maps give constraints for λ , although they are not very sensitive to its choice.

We tested the map sensitivity to the adopted bin size in the data and in the simulations. Adopting $\Delta t = 2^{-9}$ s (i.e. the minimal bin size available in analyzed PCA data set) the noise in the lightcurves (and in the power spectrum) increased but the maps were barely changed, as already noticed by Liszka, Pacholczyk & Stoeger (2000b).

5.3 Maps for lightcurves simulated in the frequency domain

An additional effort was undertaken in order to compare our simulations to the results coming from the Timmer & König (1997) approach (TK). Namely, their method allows to obtain a simulated lightcurve from the PSD of a given shape.

Since a typical PSD of Cyg X-1 is often well described by a power-law with two breaks and the three slopes of 0, 1 and 2, we decided to generate first a TK lightcurve for such a power spectrum. The break frequencies were set at 0.1 Hz and 10 Hz, correspondingly, and again, randomly selected 60 s sequence from 1000 s long time-series ($\Delta t = 0.025$ s) was selected for a closer investigation in the 1–10 Hz range.

In result we found that the wavelet maps reveal almost no patterns of variability at the level of significance greater than 90%. We estimated the κ level for 20 s time-series at only a few per cent. Only a few peaks (1–3) were able to reach the significance of 99%.

The same method and approach were used by us to generate the power spectrum assuming the shape of the underlying variability due to a Lorentzian damping. We followed the numbers given in Section 5.1 to perform simulations. As an outcome, surprisingly we found a very good agreement of the wavelet peak properties comparing to the results obtained from the wavelet maps for the (9) lightcurve. That makes these two techniques essentially equivalent in the sense of the wavelet map results.

In none of the performed TK simulations we notice any chains of features with a systematically increasing frequency along the time axis.

5.4 Morlet wavelet with non-standard parameters and other wavelet shapes

Following the most recent analysis of De Moortel, Mundat & Hood (2004) we tried to increase the time resolution at the expense of frequency resolution by adopting smaller val-

ues of $2\pi\nu_0$. We constructed the Morlet wavelet map both for the data (see Fig. 10, top panel) and for the simulated lightcurve (map not shown) using $2\pi\nu_0 = 3$. However, in this case we loose the resolution in frequency. Features become more elongated. Again, no pattern in frequency evolution can be seen. The extension of the peaks in the time domain decreased. A systematic difference between the observed and the simulated lightcurve with respect to the number of localized peaks and the extension of active periods remains. Conversely, an attempt in adopting the Morlet parameter $2\pi\nu_0 > 6$ returned in more precise frequency resolution of existing features at the expense of their time localization (map not shown). Also in this case, the statistics for the map did not change for the advantage of adopting Morlet function with $2\pi\nu_0 > 6$ ².

We also tried to apply two other wavelet shapes: a Marr and a Paul wavelet. Marr gave a very poor resolution in frequency both for the data (Fig. 10, bottom panel) and for the simulated lightcurve (map not shown), even worse than Morlet wavelet with $2\pi\nu_0 = 3$. Most of the peaks were so elongated that they extended beyond the studied frequency range, making this wavelet rather useless for the studied lightcurves. However, it indicated a fast disappearance of the peaks, in time-scales shorter than 0.3 s. Also the systematic difference between the observed and the simulated lightcurve was again seen: activity periods in Cyg X-1 covered larger fraction of time than in the simulated time-series.

The Paul wavelet (Fig. 10, middle panel) had effective properties similar to the Morlet wavelet with $2\pi\nu_0 = 3$. Therefore, the use of the canonical Morlet shape with $2\pi\nu_0 = 6$ seems to be indeed the most profitable in the context of the X-ray lightcurves.

5.5 Applicability of a single Lorentzian model to the failed transition state

Our wavelet analysis generally supports the interpretation of Cyg X-1 variability during the failed state transition as damped oscillations with fixed underlying frequency. Additional support comes from the recent paper by Feng, Zhang & Li (2004). They apply a different technique to analyze the lightcurve of Cyg X-1 (*w* spectral analysis) which is sensitive to the shortest time-scales present in the system. The resulting time-scales for the hard and the intermediate state are of the same order as the damping time-scale of the Lorentzian, consistent with the extension of the detected features on our wavelet maps.

Simulated lightcurves gave maps quantitatively similar to the maps obtained from the Cyg X-1 lightcurve. The observed PSD contains an excess of power at higher frequencies (modeled by P03 as an additional Lorentzian peak). Simulated lightcurves did not contain this additional high frequency input but still reproduced the maps properly so the dominant Lorentzian is responsible for the character of the variability both in the frequency domain and in the time-frequency domain.

² Please note that Morlet wavelet with $2\pi\nu_0 < 5$ and > 6 does not meet admissibility condition (Section 3.2.1) and its usage can be justified only for non-quantitative analysis.

5.6 Dominating PSD components in hard, soft and failed soft state

Our results give a strong support to the interpretation of the PSD through Lorentzian peak during the failed state transition. It means that in general case we most probably deal with three main *physical* components of the PSD with the following properties (Nowak 2000; P03):

- Power law component ν^{-1} : this component dominates the PSD at $\nu < 10^{-5}$ Hz (Reig, Papadakis & Kyklafis 2002), it extends up to 15–20 Hz when the source is in soft state, it extends into the region $\nu \sim 10^{-3}$ –10 Hz but with suppressed amplitude during the transition state and it practically disappears in the hard state;
- Lorentzian peak L_1 : present in the hard state but its amplitude strongly decreases during the transition state, accompanied with the rise of the power law in high frequency range;
- Lorentzian peak L_2 : suppressed only when the soft state is reached; ratio of the two Lorentzian frequencies is constant (~ 7) although the frequency can change in long time-scale up to a factor of 4.

Results for the coherence function and the Fourier time delays support the view that both Lorentzians are generally highly coherent, also between themselves (Nowak et al. 1999) but when one of the peaks disappears in the failed state transition, the mean time delay between 2–4 keV and 8–13 keV increases to 8 ms (a typical value if measured at ~ 3 Hz), and the coherence in 3–10 Hz band drops to 0.6 (P03). Similar properties were observed by Cui et al. (1997b) (e.g. 30.05.1996) when the source was on its way to the completed transition to soft state.

These components seem to be critical for our understanding of the nature of the observed variability although exact fits to the data generally require more components.

5.7 Physical interpretation of the X-ray variability

5.7.1 Power Law component ν^{-1} : propagating disk oscillations filtered at the transition radius

There are several independent arguments in favor of the hypothesis that the ν^{-1} power law component of the PSD is related to the presence of the cold disk. This component is exclusively responsible for the observed variability when Cyg X-1 is in the soft state, i.e. radiation spectrum is dominated by the disk emission and we see the relativistically broadened iron $K\alpha$ line which gives constraints for the cold disk inner radius (e.g. Di Salvo et al. 2001). The time-scales involved cover uniformly a large range, including time-scales as long as years which are naturally expected in the outer disk. However, there were two puzzles which were not initially understood. First, what we see is *not the variable disk emission*, since the direct disk emission is roughly unchanged but *variable Compton component* (Churazov, Gilfanov & Revnivtsev 2001; Maccarone & Coppi 2002). Second, the energy contained in the longest time-scale variability is considerable while the gravitational energy at the outer edge of the disk is small.

The model which successfully explains the situation is the scenario of propagating perturbations. The idea was

nicely outlined by Lyubarskii (1997), although some basic ideas were already contained in the automaton model of Mineshige et al. (1994). More sophisticated approach was developed by King et al. (2004). In this model local perturbations form in the disk as a result of the action of the magnetorotational instability (MRI; Balbus & Hawley 1991). Characteristic frequencies of these perturbations at a give radius r are somewhat lower than the local Keplerian frequency and can be expressed as:

$$\nu_{\text{mag}} = 20 \left(\frac{5.5}{k_{\text{mag}}} \right) \left(\frac{3R_{\text{Schw}}}{r} \right)^{3/2} \left(\frac{20M_{\odot}}{M} \right) \text{ [Hz].} \quad (14)$$

Most of the authors argued that the inner radius of the disk in the soft state is of order of $3 R_{\text{Schw}}$ (e.g. Frontera et al. 2001 give $6_{-0}^{+4} R_g$, where $R_g = 0.5R_{\text{Schw}}$) and we adopted this value as a convenient unit. The characteristic frequency at this radius reproduces the observed PSD frequency break at 20 Hz in the soft state when $k_{\text{mag}} = 5.5$. The factor of 2π was included, i.e. $\nu = \Omega/(2\pi)$. Those perturbations propagate inward, to the region where dissipation and the production of the hard X-ray emission proceeds. Therefore, the accretion rate at the inner dissipation region has a memory of all time-scales present in the disk at all radii.

When the source proceeds from a soft state to a hard state, the power law component is not seen at time-scales shorter than 10^{-5} – 10^{-3} Hz. We cannot relate this change to a change of the disk inner radius since this would require a change of the radius by a factor of 10^3 – 10^4 . Analysis of the data suggest much lower values; e.g. ~ 5 – $35 R_{\text{Schw}}$ (di Salvo et al. 2001), $10_{-4}^{+5} R_g$ (Frontera et al. 2001) or $\sim 100 R_g$ (Gilfanov, Churazov & Revnivtsev 2000). However, due to a different treatment of the Compton thickness of the inner disk, the values of the radii quoted above should be considered here with a caution.

However, a natural explanation of this change is found if we adopt the *strong ADAF principle* after Narayan & Yi (1995). This is a statement which tells that *whenever an ADAF can form, it does form*. The consequence of this assumption is that for a given value of the transition radius, r_{tr} , only one value of the accretion rate is possible. This fact automatically leads to filtering all time-scales in the momentary accretion rate shorter than a local viscous time-scale. If the perturbed accretion rate is somewhat larger than allowed by a current position of the transition radius, the matter accumulates near r_{tr} while the accretion rate in the inner flow is unperturbed. Mass accumulation, if persisting for long enough, leads to a build-up of a cold disk in part of the region previously occupied by the inner hot flow. The position of the transition radius moves in, and after this change an inner hot flow can transmit mass at higher rate, appropriately to the new position of r_{tr} . Alternatively, if the perturbed accretion rate in the disk is somewhat lower than current r_{tr} , the inner hot flow still persists with the same accretion rate at the expense of the cold disk. Finally, the cold material is used up, the transition radius moves out to the new position, and the accretion rate in the inner flow decreases in agreement with new r_{tr} . Since both the removal and the buildup of the cold disk happens in a local viscous timescale all variations in the accretion rate slower than that are transmitted while faster variations are damped. The fastest timescale for a transition from a hard to a soft state is also given by a

viscous time-scale,

$$\tau_{\text{visc}} = 1.5 \times 10^3 \left(\frac{0.01}{\alpha} \right) \left(\frac{0.08r}{h} \right)^2 \left(\frac{r}{50R_{\text{Schw}}} \right)^{3/2} \times \\ \times \left(\frac{M}{20M_{\odot}} \right) \text{ [s]} \quad (15)$$

and it is observationally constrained to be of order of a day, or a fraction of a day, consistent with the time-scale 10^{-3} – 10^{-5} Hz. Here we assumed the expected ratio of the disk thickness to the radius, h/r of order of 0.08 and $\alpha = 0.01$ after King et al. (2004), for the scaling purposes.

This picture gives a strong observational support to the *strong ADAF principle*. An independent argument for this kind of behavior was also found by Czerny, Różańska & Kuraszkiewicz (2004) from the study of the constraints for an inner radius from Broad Line Region in active galactic nuclei.

During the transition state the accretion rate is most probably much more strongly enhanced than during the hard state perturbations. Observations show a sudden decrease in the inner radius. For example, on 1996.05.30, when the state was yet similar to the failed state transition, the inner radius was estimated to be $9_{-4}^{+13} R_{\text{Schw}}$ (Gierliński et al. 1999). However, we can suspect that the material piles up rapidly. Instead of smooth motion of the transition radius clumps of the cold material possibly enter the inner hot flow region and accrete. Such a direct accretion of a cold phase may (i) explain why during the transition, including failed transition state, the short time-scale perturbations in the accretion flow start to propagate inward, (ii) cold moving blobs provide additional source of soft photons for Comptonization which disrupt the high coherence seen during the hard state.

It still remains to explain what kind of instability leads to the disk destruction when ADAF solution is possible. An interesting scenario is discussed by Spruit & Deufel (2002), but it requires the initial existence of the hot ions. It may give a hint why we observe a strong hysteresis effect in some sources but not in Cyg X-1. This hysteresis (see e.g. Miyamoto et al. 1995; Meyer-Hofmesiter, Liu & Meyer 2005; Zdziarski et al. 2004) leads to a transition from soft to hard state at much lower accretion rate than the transition from hard to soft state. In the soft state of Cyg X-1 significant fraction of emission is of non-thermal origin. Hot ions are always there, and the mechanism of Spruit & Derfel (2002) may operate while we need another mechanism for sources which do not show any hot plasma in the soft state.

5.7.2 Lorentzian peaks L_1 and L_2 : MRI and dynamical pulsations of the inner ion torus

The two Lorentzian peaks dominating the hard state are expected to be related to the inner ion torus. The constant ratio between their frequencies strongly suggest that we see two kinds of variability coming from the same medium.

Since the inner hot flow must transport the material the same MRI instability is expected to be operating. Since the inner flow is expected to be geometrically thick, instability has more global character there, and the dominant frequency is likely to be determined by the transition radius. This frequency still should be roughly reproduced by equation (14):

$$\nu_1 = 20 \left(\frac{5.5}{k_{\text{mag}}} \right) \left(\frac{3R_{\text{Schw}}}{r_{\text{tr}}} \right)^{3/2} \left(\frac{20M_{\odot}}{M} \right) \text{ [Hz].} \quad (16)$$

When the second Lorentzian peak is at 1.7 Hz, the first peak is at 0.25 Hz (P03), and such a frequency is reproduced for a reasonable value $r_{\text{tr}} = 55R_{\text{Schw}}$. In general, the position of the Lorentzian varies. Revnivtsev, Gilfanov & Churazov (2001) showed that the corresponding peak in the power spectrum of GX 339-4, described as quasi-periodic oscillation (QPO), strongly correlates with the other spectral properties of this source, supporting its connection with the change of the transition radius.

Higher frequency variations are likely to represent the dynamical pulsation of the inner hot flow, or traveling sound waves. Global oscillations of this medium, modeled as a torus, were studied in a number of papers (e.g. Abramowicz, Calvani & Nobili 1983; Giannios & Spruit 2004; Montero, Rezzolla & Yoshida 2004). The typical frequencies of p -modes depend on the details of the model (e.g. assumed radial distribution of the angular momentum) but they are roughly of the order of the Keplerian frequency at the outer edge of the torus (Rezzolla, Yoshida & Zanotti 2003). The excitation of the modes is due to a radiative interaction of the disk and the torus, while the synchrotron emission provides the damping mechanism (Giannios & Spruit 2004).

The expected frequency of this mode is roughly:

$$\nu_2 = 1.62 \left(\frac{50R_{\text{Schw}}}{r_{\text{tr}}} \right)^{3/2} \left(\frac{20M_{\odot}}{M} \right) \text{ [Hz]} \quad (17)$$

so the value of the transition radius $\sim 50R_{\text{Schw}}$ gives the value of the frequency roughly corresponding to the observed frequency of the Lorentzian, 1.7 Hz.

During the failed transition state the first Lorentzian peak is strongly damped, and a power law components is partially rebuilt, as discussed in Section 5.7.1. If the first Lorentzian peak is connected with MRI instability, the exchange of power between a power law component and the first Lorentzian is natural. Decreased MRI instability in the inner flow suppress the accretion of the hot material and the accretion proceeds predominantly through cold blobs. It is an interesting question whether the presence of the cold blobs prevent MRI instability or the absence of hot material accretion forces the cold phase to take over but the eventual compensation of the two mechanisms is quite intuitive. Apparently, dynamical pulsations persist as long as the hot inner torus is still there. If a transition to a soft state is completed, this phase finally disappears.

The suggested picture may be too simple since actually a number of instabilities may operate in the accretion flow (e.g. Menou, Balbus & Spruit 2004 and the references therein) but we consider our interpretation as a plausible and attractive scenario. Clearly, quantitative models would be needed to work out the detailed predictions.

Observationally, an insight may come from the presence of rapid, very energetic events reported by Gierliński & Zdziarski (2003) both during soft and hard state. It is interesting that a soft state flare no. 13, studied in detail by these authors, was found to be well described by damping time-scale (after the peak) of $\tau = (21 \pm 6)^{0.7 \pm 0.1}$ ms, i.e. $\tau \simeq 0.07$ s. This damping time-scale is the same as the damping time-scale of the L_2 Lorentzian, which may indi-

cate that damping is related to magnetic field reconnections. Same event observed in the hard state yielded much longer damping time-scale, ~ 0.32 s which in turn roughly coincides with the damping time-scale of the first Lorentzian, L_1 . Although the exact origin of the flares is not known, one takes into account sudden conversion of energy accumulated in the disk into magnetic heating of a hot plasma or fast release of energy due to magnetic field reconnection in the flares hung above the disk (Gierliński & Zdziarski 2003 and references therein). The difference between the hard state and the soft or failed transition state may be due to the absence of the cold material in the former case. Therefore, in the hard state the large scale magnetic loops exist within the torus, while in the soft state or failed transition state magnetic field lines are partially frozen into the cold disk or cold blobs.

5.8 Wavelet analysis as a tool for tracing accreting matter onto black-holes?

It is tempting to associate the observed puzzling chain of peaks in Fig. 7 (mentioned already by us in Section 4.1) with a systematic trend. Closer look in this figure shows up, in fact, not one but two sequences of peaks roughly of the same slope. The first one, most prominent, extends between 383–391 s, whereas the second one between 389–397 s. Comparison of wavelet map with corresponding PCA lightcurve reveals that all wavelet features are associated with some peaks occurring in the same moments in the time-series, as expected. In addition, a careful inspection of all 20 s long sequences of the PCA observation uncovers more similar chains of the same slope. Unfortunately, their number is low i.e. ~ 14 per whole lightcurve, each one of duration ≤ 7 s. Interestingly, we did not find similar chains of evolution from lower to higher frequencies in the simulated data.

The time–frequency evolution of some features is not totally unexpected. Both the hot ion torus material and cold clumps flow onto the black-hole, in the direction of decreasing Keplerian time-scales. We can witness a manifestation of the single events like a sequence of magnetic field reconnections in an inflowing material. Theoretically, this issue were discussed already by Stoeger (1980), however, his considerations were mostly appropriate for events taking place below the marginally stable orbit. Here, it seems that observed features between 1–10 Hz correspond rather to the range of 69 – $15 R_{\text{Schw}}$.

If these enigmatic chains of oscillations are related somehow to the processes of X-ray emission coming from the material accreting onto black-holes, then, in our opinion, a wavelet analysis may become a promising tool in their spotting. However, any judgement on the reality and physical origin of the observed *trends* can be only done after much more quantitative analysis. The number of the detected *chains* must be large and statistically significant.

6 CONCLUSIONS

For the first time, we applied the wavelet multi-resolution approach in order to perform the complex studies of aperiodic X-ray variability of Cyg X-1. Considered data set corresponded to its failed state transition on 1999.12.05. On that day, the Fourier power spectrum revealed a broad-band

peak between ~ 1 – 10 Hz, well described by a single Lorentz function of unclear origin. On the contrary to the Fourier method, the wavelet analysis provided an excellent inspection of the frequency content of the signal as well as allowed for simultaneous spotting the time evolution of the extracted features.

Our results can be summarized as follows:

- Cyg X-1 lightcurve analyzed in the time–frequency plane contained randomly appearing flare-like structures of duration ~ 0.5 s and of the average median of the peak frequency width $\Delta \log \nu_p \simeq 0.14$;
- observed Lorentzian shape forms through summation of these time-localized structures;
- most of the Cyg X-1 lightcurve properties are well reproduced by the simulated lightcurve composed of a series of randomly occurring flares. In our model, each flare was described as a damped oscillator with variable amplitude and phase but fixed excitation frequency and time-scale of decay;
- Cyg X-1 wavelet maps may show insignia of an inflow while the maps representing the simulated lightcurve do not seem to show similar tendency. However, no statistical significance was assigned to this hypothesis.

ACKNOWLEDGMENTS

The work dedicated in memory of Prof. Edward Wilk. We thank Chris Torrence for many helpful and friendly discussions on wavelets, and the referee and Piotr Źycki for valuable remarks. The wavelet software was provided by Christopher Torrence and Gilbert P. Compo and it is available at <http://paos.colorado.edu/research/wavelets>. Part of this work was supported by grants 2P03D00322 and PBZ-KBN-054/P03/2001 of the Polish State Committee for Scientific Research. We also acknowledge the use of data obtained through the HEASARC online service provided by NASA/GSFC.

REFERENCES

Abramowicz M., Calvani M., Nobili L., 1983, *Nat.*, 302, 597

Angelini L., White N., Stella L., 1992, *IAU Circ.* No. 5580

Aschwanden M.J., Kliem B., Schwarz U., Kurths J., Dennis B.R., Schwartz R.A., 1998, *ApJ*, 505, L941

Balbus S., Hawley J.F., 1991, *ApJ*, 376, 214

Barreiro R.B., Hobson M.P., 2001, *MNRAS*, 327, 813

Belloni T., Hasinger G., 1990, *A&A*, 227, L33

Bolton C. T., 1972, *Nature*, 235, 271

Böttcher M., Liang E.P., 1999, *ApJ*, 511, L37

Bowyer S., Byram E.T., Chubb T.A., Friedman H., 1965, *Science* 147, 394

Bradt H.V., Rothschild R.E., Swank J.H., 1993, *A&AS*, 97, 355

Churazov E., Gilfanov M., Revnivtsev M., 2001, *MNRAS*, 321, 759

Cohen, L. 1995, Time-frequency analysis, Englewood Cliffs, NJ: Prentice-Hall

Combes J.M., Grossmann A., Tchamitchian P., 1989, eds. Wavelets, Time-Frequency Methods and Phase Space, 1st Int. Wavelet Conf., Marseille, Dec. 1987, Inverse Probl. Theoret. Imaging, Springer

Cui W., Heindl W.A., Rothschild R.E., Zhang S.N., Jahoda K., Focke W., 1997a, *ApJ*, 474, L57

Cui W., Zhang S.N., Focke W., Swank J.H., 1997b, *ApJ*, 484, 383

Czerny B., Różańska A., Kuraszkiewicz J., 2004, *A&A*, 428, 39

Daubechies I., 1992, Ten Lectures on Wavelets, Philadelphia PA: Society for Industrial and Applied Mathematics, 357pp

De Moortel I., Munday S.A., Hood A.W., 2004, *SoPh*, 222, 203

Di Salvo T., Done C., Źycki P.T., Burderi L., Robba N.R., 2001, *ApJ*, 547, 1024

Escalera E., MacGillivray H.T., 1995, *A&A*, 298, 1

Farge M., 1992, *AnRPFM*, 24, 395

Feng H., Zhang S.-N., Li T.-P., 2004, *ApJ*, 612, L45

Flandrin P., 1999, Time-Frequency/Time-Scale Analysis, Academic Press

Freeman P.E., Kashyap V., Rosner R., Lamb D.Q., 2002, *ApJS*, 138, 185

Frick P., Galyagin D., Hoyt D.V., Nesme-Ribes E., Schatten K.H., Sokoloff D., Zakharov V., 1997, *A&A*, 328, 670

Fritz T., Bruch A., 1998, *A&A*, 332, 586

Frontera F., Palazzi E., Zdziarski A.A., Haardt F., Perola G.C., Chiappetti L., Cusumano G., Dal Fiume D., Del Sordo S., Orlandini M., 2001, *ApJ*, 546, 1027

Giannios D., Spruit H.C., 2004, *A&A*, 427, 251

Gierliński M., Zdziarski A.A., Poutanen J., Coppi P.S., Ebisawa K., Johnson W.N., 1999, *MNRAS*, 309, 496

Gierliński M., Zdziarski A.A., 2003, *MNRAS*, 343, L84

Gies D.R., Bolton C.T., 1986, *ApJ*, 304, 371

Gilfanov M., Churazov E., Revnivtsev M., 2000, *MNRAS*, 316, 923

Gleissner T., Wilms J., Pottschmidt K., Nowak M.A., Staubert R., 2004, *A&A*, 414, 1091

Gray D.F., The observation and analysis of stellar photospheres, 1976, John Wiley & Sons, A Wiley-Interscience Publication

Grossman A., Morlet J., 1984. Decomposition of Hardy functions into square integrable wavelets of constant shape. Society for Industrial and Applied Mathematics Journal on Mathematical Analysis, 15:732-736

Herrero A., Kudritzki R.P., Gabler R., Vilchez J.M., Gabler A., 1995, *A&A*, 297, 556

Irastorza I.G., Morales A., Cebría S., Garc E., Morales J., Ortiz de Solorzan A., Osetrov S.B., Puimedo J., Sarsa M.L., Villar J.A., 2003, *APh*, 20, 247

King A.R., Pringle J.E., West R.G., Livio M., 2004, *MNRAS*, 348, 111

Lehto H.J., 1989, in ESA, The 23rd ESLAB Symposium on Two Topics in X Ray Astronomy. Volume 1: X-Ray Binaries, p, 499-503

Liszka L., Pacholczyk A.G., Stoeger W.R., 2000a, *ApJ*, 540, 122

Liszka L., Pacholczyk A.G., Stoeger W.R., 2000b, *A&A*, 354, 847

Lyubarskii Yu.E., 1997, *MNRAS*, 292, 679

Maccarone T., Coppi P.S., 2002, *MNRAS*, 335, 465

Menou K., Balbus S.A., Spruit H.C., 2004, *ApJ*, 607, 564

Meyer-Hofmeister E., Liu B.F., Meyer F., 2005, *A&A*, 432, 181

Mineshige S., Ouchi B., Nishimori H., 1994, *PASJ*, 46, 97

Miyamoto S., Kitamoto S., Iga S., Negoro H., Terada K., 1992, *ApJ*, 391, L21

Montero P.J., Rezzolla L., Yoshida S., 2004, *MNRAS*, 354, 1040

Miyamoto S., Kitamoto S., Hayashida K., Egoshi W., 1995, *ApJ*, 442, L13

Narayan R., Yi I., 1995, *ApJ*, 452, 710

Nowak M.A., Wagoner R.V., 1995, *MNRAS*, 274, 37

Nowak M.A., Vaughan B.A., Wilms J., Dove J.B., Begelman M.C., 1999, *ApJ*, 510, 874

Nowak M.A., 2000, *MNRAS*, 318, 361

Paul T., 1984, *J. Math. Phys.*, 25, 11

Pottschmidt K., Wilms J., Nowak M.A., Pooley G.G., Gleissner T., Heindl W.A., Smith D.M., Remillard R., Staubert R., 2003, *A&A*, 407, 1039

Poutanen J., Fabian A.C., 1999, *MNRAS*, 306, L31

Press W.H., Teukolsky S.A., Vetterling W.T., Flannery B.P.,

1992, Numerical recipes in FORTRAN. The art of scientific computing, Cambridge: University Press, 2nd ed.

Psaltis D., 2004, in "Compact Stellar X-ray Sources", eds. W.H.G. Lewin and M. van der Klis, astro-ph/0410536

Reig P., Papadakis I., Kylafis N.D., 2002, A&A, 383, 202

Revnivtsev M., Gilfanov M., Churazov E., 2000, A&A, 363, 1013

Revnivtsev M., Gilfanov M., Churazov E., 2001, A&A, 380, 520

Rezzolla L., Yoshida S., Zanotti O., 2003, MNRAS, 344, 978

Scargle J.D., 1982, ApJ, 263, 835

Scargle J.D., Steiman-Cameron T., Young K., Donoho D.L., Crutchfield J.P., Imamura J., 1993, ApJ, 411, L91

Spruit H.C., Deufel B., 2002, A&A, 387, 918

Steiman-Cameron T.Y., Scargle J.D., Imamura J.N., Middleditch J., 1997, ApJ, 487, 396

Stoeger W.R., 1980, MNRAS, 190, 715

Sutherland P.G., Weisskopf M.G., Kahn S.M., 1978, ApJ, 219, 1024

Szatmary K., Vinko J., Gal J., 1994, A&AS, 108, 377

Terrell N.J. Jr., 1972, ApJ, 174, L35

Timmer J., König M., 1995, A&A, 300, 707

Torrence C., Compo G.P., 1998, BAMS, 79, 61

Uttley P., McHardy I.M. 2001, MNRAS, 323, L26

Uttley P., 2004, MNRAS, 347, L61

van der Klis M., 1989, in Timing Neutron Stars, eds. H. Ogelman and E. P. J. van den Heuvel (Dordrecht: Kluwer), 27

Vaughan S., Edelson R., Warwick R.S., Uttley P., 2003, MNRAS, 345, 1271

Vio R., Wamsteker W., 2002, A&A, 388, 1124

Walborn N., 1973, ApJ, 179, L123

Webster B.L., Murdin P., 1972, Nature, 235, 37

Zdziarski A.A., Gierliński M., Mikołajewska J., Wardziński G., Smith D.M., Harmon A.B., Kitamoto S., 2004, MNRAS, 351, 791

Zhang W., Jahoda K., Swank J.H., Morgan E.H., Giles A.B., 1995, ApJ, 449, 930

Ziółkowski J., 2005, MNRAS, 358, 851

Życki P.T., 2002, MNRAS, 333, 800

Życki P.T., 2003, MNRAS, 340, 639

APPENDIX A: DISCRETE FORM OF CWT IN TERMS OF FOURIER TRANSFORM

Let us express a continuous wavelet transform as the convolution of the Fourier transforms of the lightcurve and wavelet function in the following way:

$$w_{a,b} = \int_{-\infty}^{\infty} \hat{x}(\nu) \hat{\psi}_{a,b}^*(\nu) d\nu. \quad (A1)$$

The Fourier transform of $\psi_{a,b}$ is given by:

$$\hat{\psi}_{a,b}(\nu) = \frac{1}{\sqrt{a}} \int_{-\infty}^{\infty} \psi\left(\frac{t-b}{a}\right) e^{-i2\pi\nu t} dt. \quad (A2)$$

Substituting $(t-b)/a$ by η equation (A2) evaluates into:

$$\hat{\psi}_{a,b}(\nu) = \sqrt{a} e^{-i2\pi\nu b} \int_{-\infty}^{\infty} \psi(\eta) e^{-i2\pi a\nu \eta} d\eta \quad (A3)$$

where a constant component was separated out. As one can see, an integral expression can be considered as the Fourier transform of a wavelet function where $2\pi a\nu$ is a rescaled angular frequency. Thus it is possible to denote (A3) shortly:

$$\hat{\psi}_{a,b}(\nu) = \sqrt{2\pi a} e^{-i2\pi\nu b} \hat{\psi}(2\pi a\nu) \quad (A4)$$

and therefore a CWT as the inverse Fourier transform of the product:

$$w_{a,b} = \sqrt{2\pi a} \int_{-\infty}^{\infty} \hat{x}(\nu) \hat{\psi}^*(2\pi a\nu) e^{i2\pi\nu b} d\nu \quad (A5)$$

where complex conjugate of the Fourier transform of ψ function was taken into account.

A discrete Fourier transform of x_k is given by

$$\hat{x}_j = N_{\text{obs}}^{-1} \sum_{k=0}^{N_{\text{obs}}-1} (x_k - \bar{x}) e^{-i2\pi j k / N_{\text{obs}}} \quad (A6)$$

where j denotes a frequency index. Performing a discrete notation of the time-shifting factor as $b = k\Delta t$ where Δt stands for the sampling time of a lightcurve, one can write down a *discrete form of continuous wavelet transform in terms of the Fourier transform* as:

$$w_k(a) = \left(\frac{2\pi a}{\Delta t}\right)^{1/2} \sum_{j=1}^{N_{\text{obs}}} \hat{x}_j \hat{\psi}^*(2\pi a\nu_j) e^{i2\pi\nu_j k \Delta t} \quad (A7)$$

where frequency ν_j equals:

$$\nu_j = \begin{cases} j/(N_{\text{obs}}\Delta t) & \text{for } j \leq N_{\text{obs}}/2 \\ -j/(N_{\text{obs}}\Delta t) & \text{for } j > N_{\text{obs}}/2 \end{cases} \quad (A8)$$

and the factor $(2\pi a/\Delta t)^{1/2}$ ensures that wavelet will keep the same energy at every scale a . Because of the finite duration of the signal, the proper choice of scales must be done. The largest scale would correspond to the lightcurve span of T whereas the smallest one to ought to be an equivalent of the Fourier Nyquist frequency, i.e. $a_0 = 2\Delta t$. In fact, a selection of scales in this region can be chosen arbitrarily with a step in scale not smaller than a_0 . However, in case of very fine signal when a few decades of scales are wished to be covered, one can build the wavelet transform choosing:

$$a_m = a_0 2^{m\Delta m} \quad m = 0, \dots, M \quad (A9)$$

where

$$M = \Delta m^{-1} \log_2(N_{\text{obs}}\Delta t a_0^{-1}) \quad (A10)$$

(TC98) and thus rewriting (A7) in the following way:

$$w_k(a_m) = \left(\frac{2\pi a_m}{\Delta t}\right)^{1/2} \sum_{j=1}^{N_{\text{obs}}} \hat{x}_j \hat{\psi}^*(2\pi a_m \nu_j) e^{i2\pi\nu_j k \Delta t}. \quad (A11)$$

This paper has been typeset from a TeX / $\text{L}\text{AT}\text{E}\text{X}$ file prepared by the author.